Available online at www.sciencedirect.com

SciVerse ScienceDirect

Acta Materialia 60 (2012) 1418–1432

Acta MATERIALIA

www.elsevier.com/locate/actamat

# Quasi-static and dynamic response of explosively consolidated metal–aluminum powder mixtures

C.T. Wei [a], E. Vitali [c], F. Jiang [a], S.W. Du [b], D.J. Benson [a], K.S. Vecchio [a], N.N. Thadhani [b], M.A. Meyers [a,*]

[a] University of California, San Diego, La Jolla, CA 92093, USA
[b] Georgia Institute of Technology, Atlanta, GA 30332, USA
[c] Lawrence Livermore National Laboratory, Livermore, CA 94550, USA

Received 16 August 2011; received in revised form 12 October 2011; accepted 16 October 2011
Available online 2 January 2012

**Abstract**

Nearly fully dense (>96% theoretical maximum density) powder mixture compacts with combinations of Nb, Ni, Mo, W, and Ta, with Al, were produced by explosive consolidation. The quasi-static and dynamic behavior and failure mechanisms were investigated experimentally and computationally. For two mixtures (Ni + Al, W + Al) the Al phase was continuous, while for the other three mixtures (Nb + Al, Ta + Al, Mo + Al), the Al phase was discontinuous. It was found that the continuous phase significantly influenced the mechanical response (in compression) and determined the fracture morphology of the compacts. Accordingly, the mixtures with continuous Al phases had the lowest compressive strength. Two distinct failure mechanisms, axial splitting and shear failure, were observed. Axial splitting occurred when the Al phase was continuous (Ni + Al, W + Al); shear failure was primarily associated with extensive deformation of the Nb, Ta and Mo continuous phases. Finite element simulations provide valuable help in interpreting the experimental results and predicting mechanical strength and failure mechanisms akin to those observed. The interfacial bonding strength is shown to be an important parameter in determining the mechanical response of the compacts.


*Keywords:* Powder consolidation; Dynamic mechanical analysis; Finite element analysis; Aluminum; Dynamic compaction

## 1. Introduction

Reactive powder mixtures have been extensively investigated due to their utilization in the synthesis of compounds that are difficult to obtain by traditional methods [1–6], tailoring the mechanical and/or chemical properties by combining different elements [7], and in providing a means to deliver energy associated with their high heat of reaction. Compacts of reactive mixtures can be manufactured by shock synthesis, combustion synthesis followed by densification, and a variety of other techniques [4–12]. These manufacturing processes generate significant strains, void collapse, shear deformation and friction between either particles or reaction products, thereby facilitating the bonding of different materials and increasing the density of the final product. There is a large variety of combinations of materials amenable to producing powder-consolidated reactive mixtures, the requirement being that the reactions have to be sufficiently exothermic. The mechanical and chemical properties of the different components in powder-consolidated reactive mixtures significantly influence the mechanical performance and structure of the mixtures [6]. By using different manufacturing processes such as shock compaction [13–15], self-propagating high-temperature synthesis (SHS) (including thermite-base SHS) [3,6,16–18], and mechanical alloying [19], a number of intermetallic compounds can be produced from the reactive mixtures [6].

The schematic sequence illustrated in Fig. 1 shows the initiation and propagation of an exothermic intermetallic

* Corresponding author. Tel.: +1 858 534 4719.
*E-mail address:* mameyers@ucsd.edu (M.A. Meyers).

1359-6454/$36.00 © 2011 Published by Elsevier Ltd. on behalf of Acta Materialia Inc.
doi:10.1016/j.actamat.2011.10.027

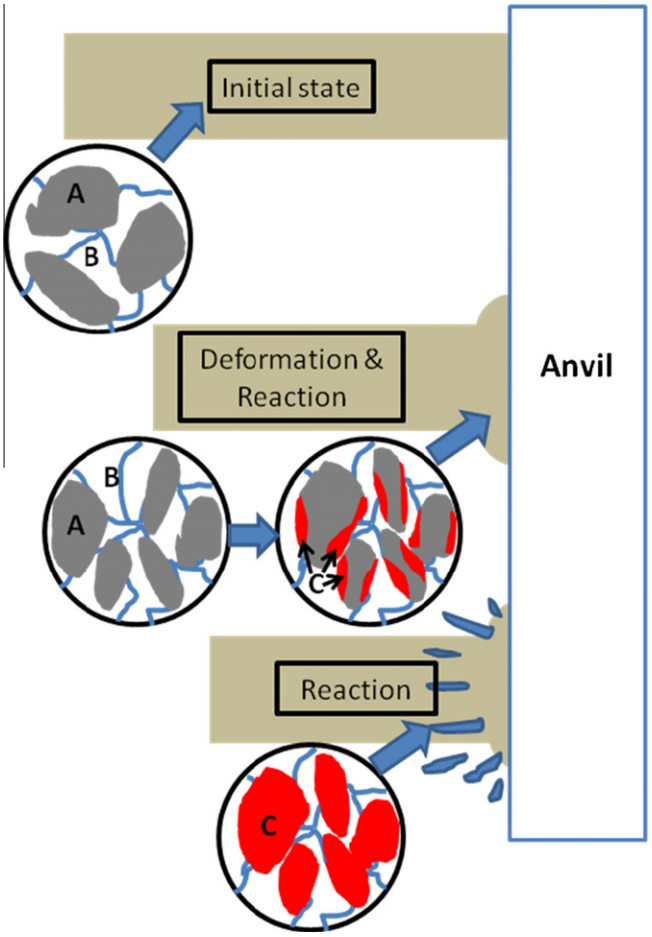


Fig. 1. Schematic showing consolidated reactive powder mixture in cylindrical configuration subjected to dynamic deformation which initiates exothermic reaction. Top: cylindrical projectile in flight; middle: impact, deformation, and initiation of reaction; bottom: propagation of reaction.

reaction caused by high-strain-rate deformation of a reactive powder mixture compact, upon its impact against a high-strength, high-rigidity anvil. This is in applications where it may be desirable for the dynamic event to trigger the sudden release of energy. There are three sequential steps in the reaction. In the initial state, the original material consisting of a densified mixture of A and B impacts the anvil at a certain velocity (Fig. 1, top). The second step shows the initiation of reaction due to impact pressure, severe lateral strain, void collapse, and friction between components (Fig. 1, middle). This can result in exothermic reactions, which release thermal energy (third step), consequently inducing sequential intermetallic reactions (Fig. 1, bottom), and delivering additional energy to the projectile–target interface.

The objective of this study was to investigate the mechanical response and failure mechanisms in powder mixture compacts produced by shock compaction, prior to their undergoing reaction. The densification pressure during explosive compaction was kept intentionally low, avoiding any significant shock-induced melting and reaction [20], while ensuring almost full densification.

## 2. Experimental methods

The reactive mixtures (Ni + Al, W + Al, Mo + Al, Nb + Al, Ta + Al) with an equivolumetric ratio, were explosively shock-consolidated to obtain near full-density compacts. The as-produced compacts were characterized experimentally and computationally in order to further our understanding of the deformation and fracture response (under quasi-static and dynamic loading) of the consolidated powder mixtures with different elemental combinations and distinct microstructures.

Commercially available elemental powders (purity higher than 98%) of Al, Ni, Nb, W, Mo, Ta, were employed to produce shock-consolidated powder mixture compacts. The distinct particle morphology and size distribution of each powder type are shown in Figs. 2 and 3. The Ni, Al, and W powders (Fig. 2a–c) have relatively homogeneous shapes and particle sizes while the Mo, Nb, and Ta (Fig. 3a–c) have arbitrary shapes and a large variety of particle sizes (from less than 1 μm diameter to ~50 μm diameter). The particle sizes of Ni, W, Al powders are in the range 30–80 μm. It should be noted that the powders with relatively small particle sizes, Nb, Ta, and Mo, are clustered due in part to the large increases of the surface area, which enhance the effect of the van der Waals attraction forces that become progressively more relevant as the grain size is decreased [21]. Thus, the particles have a spongy configuration. It will be shown later that this ultimately affects the microscopic structure of the shock-consolidated compacts.

The powders were blended in equivolumetric ratios using a V-blender, then placed into the inner tube of the double tube explosive consolidation system (Fig. 4), similar to the setup developed by Meyers and Wang [13]. This setup has a cylindrical geometry with two co-axial tubes. The detailed dimensions are shown in Fig. 4. The Al mandrel helps to prevent Mach stem effect (Fig. 4) [13]. The outer tube was surrounded by a mixture of ANFO (ammonium nitrate–fuel oil mixture) and perlite, which gave a detonation velocity of 2.6 km $s^{-1}$, yielding a calculated peak pressure in the range of 4–7 GPa [14,22]. The pressure was below the threshold for extensive interparticle melting, since the goal was not necessarily to obtain compacts with strong interparticle fusion bonding, but rather to achieve close to full densification and none or minimized reactions between the constituents. The compaction geometry was designed based on two-dimensional (2-D) computations performed using AUTODYN, which showed uniform pressure distribution at least along 70-80% of the length of the compact. After consolidation, cylindrical rods with diameter of 3 mm were machined from the middle part of compacts, parallel to the tube axis. The final microstructure in terms of particle distribution and volume fractions was determined by the cross-sectional distribution of the pressure during explosive shock consolidation, and the viscosity of each elemental particle. Observation was made in the central portion of the cross-section. The discrepancy

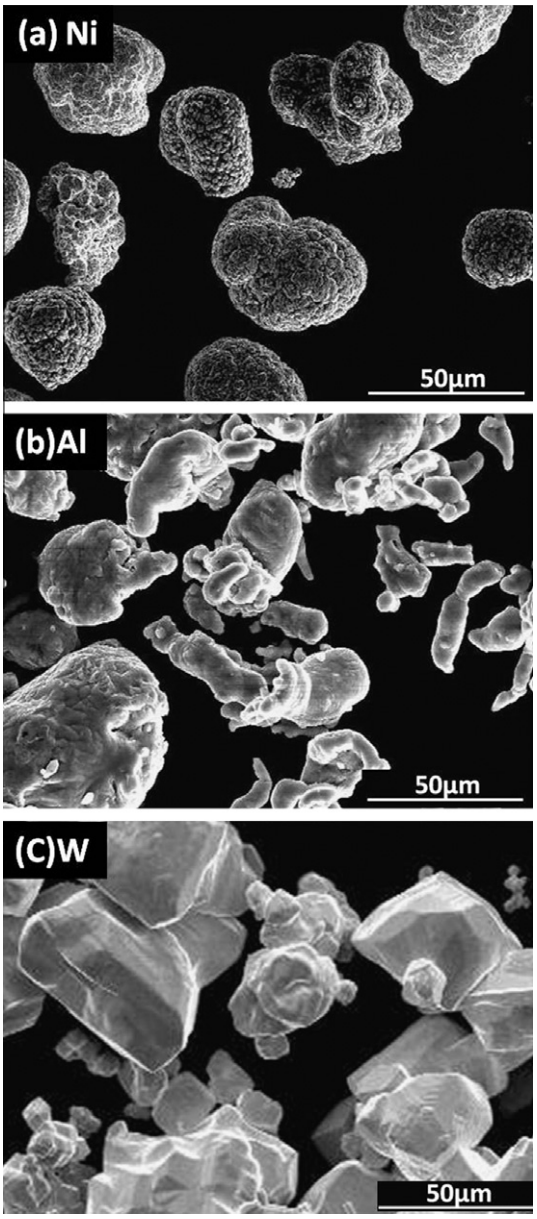


Fig. 2. SEM micrographs of the larger starting powders: (a) Ni, (b) Al, (c) W.

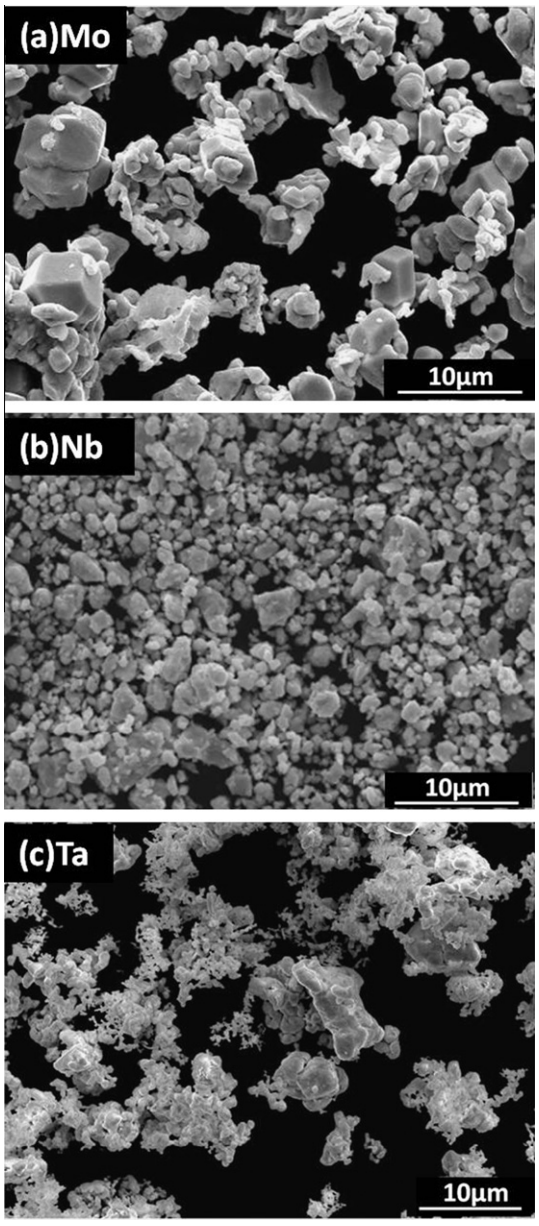


Fig. 3. SEM micrographs of the smaller (agglomerated) starting powders: (a) Mo, (b) Nb, (c) Ta.

between the initial (in the green body) and the final volume fractions (in the consolidated cylinders) is currently uncertain; however, the consistency among specific mixtures was ensured. A reasonable postulation is that the flow rate of the two particles in the mixture was differentiated, leading to a non-uniform distribution in the compact. The molar ratio, the measured Archimedean density ($\rho$) and the percentage of theoretical maximum density (TMD) for each powder mixture compact are listed in Table 1 [14]. Optical microscopy confirms that variations in microstructure (including intermetallic formation) and densities along the radius were restricted [14] in the as-produced samples.

The compacts were mechanically tested in a universal testing machine (Model Instron 3370) and split Hopkinson pressure bar. In dynamic testing, an aluminum pulse-shaper with high-work-hardening rate was applied in order to generate a long rise time and a nearly square strain rate pulse [23], which helped to ensure the equilibration of stress in the specimen and maintain a constant strain rate. Constant strain rates of $\sim 10^3$ and $2.5 \times 10^3\ s^{-1}$ were achieved by using this technique at different impact velocities.

A high-speed camera (Vision Research Phantom V710) was employed for obtaining high-resolution, time-resolvable images to study the evolution of fracture. Vickers indentation experiments were conducted for characterizing the microhardness of elemental phases within the compacts. The computational simulation code RAVEN was used for analyzing the evolution of plasticity and damage, and for comparison with experimental results. Scanning electron microscopy was conducted using a Phillips XL30

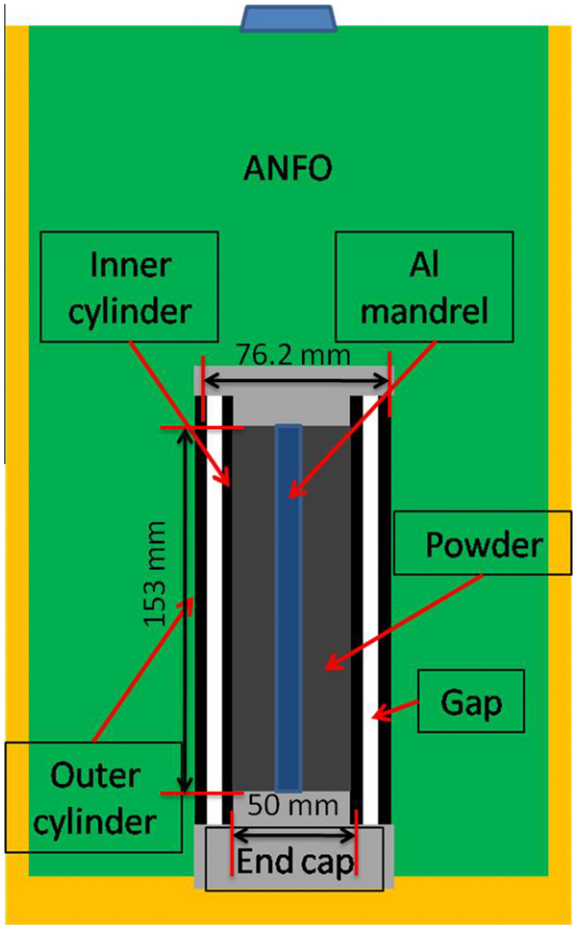


Fig. 4. Double tube explosive setup [13] for the explosive shock consolidation of powder mixtures.

ESEM and X-ray diffractometry using a Rigaku MiniFlex II. Differential thermal analysis was employed for determining the reaction temperatures upon heating the compacts at a constant rate. The recovered samples were embedded in Buehler low viscosity epoxy mixed with a hardener in order to ensure that the fracture morphologies were preserved during the polishing process.

## 3. Results and discussion

### 3.1. Compact microstructure

Fig. 5 shows scanning electron microscopy (SEM) backscattered electron images revealing the cross-sectional microstructure of the various shock-consolidated compacts. For all mixtures, the darker phase is aluminum, by virtue of its lower atomic number. The starting densities of the mixtures are in the range of 60-65% TMD. The compacts have over 96% TMD and a molar ratio close to 1:1 after explosive consolidation, which is close to the fully dense materials (Table 1). The Ni + Al compact had spheroidal Ni particles surrounded by a continuous dark-contrast Al matrix (Fig. 5a). The W + Al compact has a similar morphology to Ni + Al (Fig. 5a and b), with Al forming the continuous phase; the W particles (Fig. 5b) are more irregular and have more angular shapes, as shown in Fig. 2c. For the other compacts, the Mo, Nb or Ta particles plastically deformed and became interconnected as a continuous phase. The explanation for this difference in the compact microstructure is due to the morphology of the initial powders. The Mo, Nb, and Ta powders were agglomerated and thus surrounded and enveloped the Al powders during mixing and subsequent explosive compaction (Fig. 5c–e). In some cases the compacts might have limited intermetallic phases formed due to localized reaction during explosive shock consolidation, although no obvious reacted regions were identified in SEM images.

### 3.2. Mechanical properties

Due to the imperfections such as cracks and voids, and the varied morphologies of the initial powders in the explosively shock-consolidated compacts, the elastic, plastic and dynamic behavior of these powder-consolidated compacts show significant variation [6,24] in comparison with monolithic alloys.

The quasi-static compression test results, shown in Fig. 6a, reveal that these powder-consolidated compacts have Young's moduli varying from 37 to 91 GPa. These cylindrical samples have dimensions of 4 mm (length) × 3 mm (diameter). No extensometer was used and the results were corrected from load–displacement plots by subtracting machine effects. These values are somewhat lower than those calculated from linear interpolations, proposed by Hashin [25], based on the Young's moduli of the components.

The microindentation Vickers hardness (VHN) of each phase in the explosive shock-consolidated compacts are shown in Table 2. This enables an approximate estimate of the yield stress ($\sigma_y$) of the material through the Tabor equation: $\sigma_y = VHN/3$ [26]. By using a simple rule of mixtures for the composites [7,27], estimates of the yield stress, $\sigma_c$, can be obtained through Eq. (1):

$$\sigma_c = \sigma_m V_m + \sigma_s V_s \quad (1)$$

where $\sigma_m$ and $\sigma_s$ are respectively the yield stress of the matrix and second phase which are estimated from the

Table 1
Properties of explosively shock-consolidated compacts [6].

| Compacts | Ni + Al | Nb + Al | W + Al | Mo + Al | Ta + Al |
|---|---|---|---|---|---|
| Molar ratio | 1.483:1 (Ni:Al) | 0.908:1 (Nb:Al) | 1.026:1 (W:Al) | 1.044:1 (Mo:Al) | 0.903:1 (Ta:Al) |
| TMD (%) | 97.4% | 99.1% | 99.1% | 96.5% | 98.3% |
| $\rho$ (kg m$^{-3}$) (sample) | 5649 | 5528 | 10,903 | 6222 | 9181 |

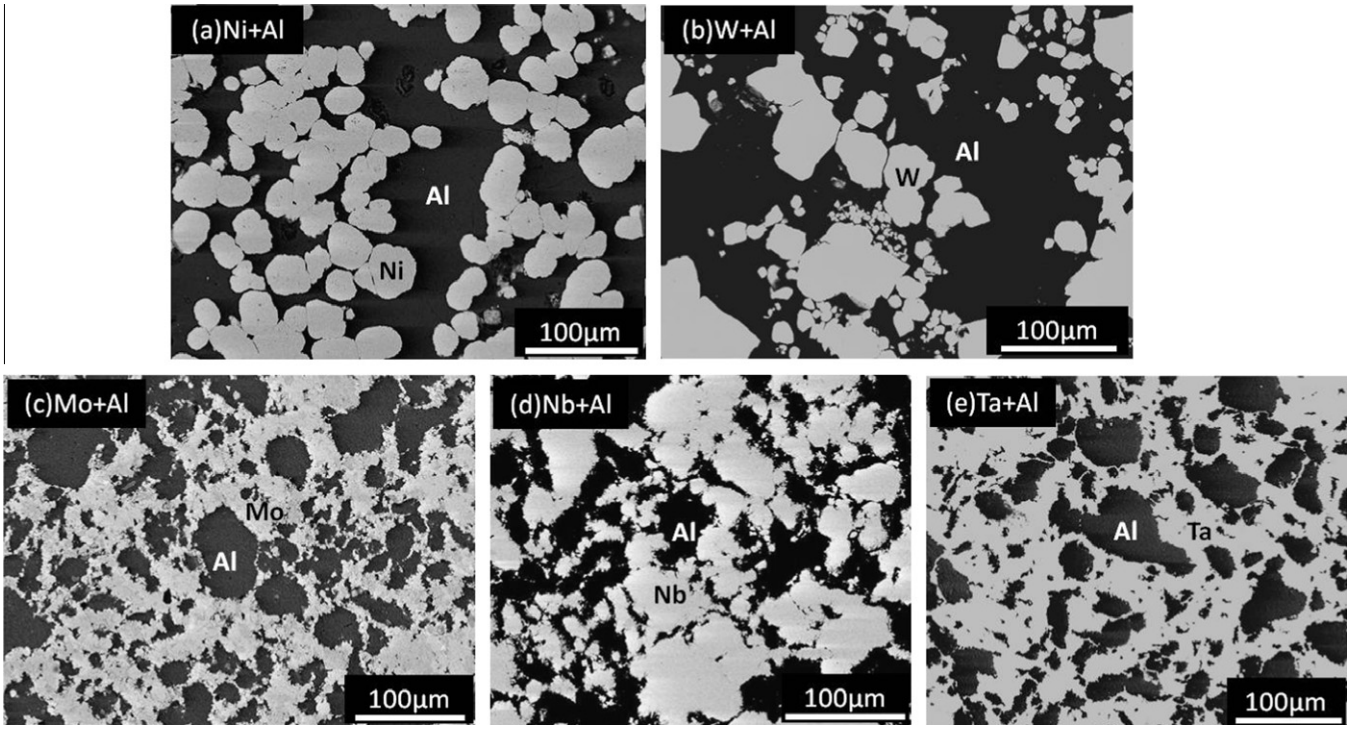


Fig. 5. Cross-sectional SEM micrographs of consolidated mixtures: (a) Ni + Al, (b) W + Al, (c) Mo + Al, (d) Nb + Al, (e) Ta + Al (the darker areas represent aluminum (BSE)). Compact densities over 96% TMD.

hardness, and $V_m$ and $V_s$ are the corresponding volume fractions shown in Table 3.

Interestingly, from the experimental measurements, the compact with hardest second phase, tungsten, has the lowest yield stress, ~240 MPa obtained from the measured quasi-static stress–strain curves (Fig. 6a). The compact with relatively softer second phase, Ta, has the highest yield stress, which is ~450 MPa. These experimental results are in contrast to the estimates from the rule of mixtures (Table 3). This inconsistency suggests that the yield stress of the explosively shock-consolidated compacts is not directly determined by the mechanical properties of the two components through Eq. (1). This will be discussed further below.

The microstructural characterization in Fig. 5 provides the possible strengthening mechanisms. It shows that the high yield strength compacts, Mo + Al, Nb + Al and Ta + Al (Fig. 5c–e), have continuous second phases composed of Mo, Nb and Ta, respectively. In contrast, the low yield strength compacts, Ni + Al and W + Al, have Al as the continuous phase. This suggests that the continuous phase in the compact determines the yield strength of the explosively consolidated powder mixture compacts. Similar results were obtained by Williamson and coworkers [28], who studied polymer-bonded composites in which crystalline polymer bonded explosives were embedded in a continuous matrix. The mechanical strength was determined primarily by the continuous phase, which acted as the binder for the explosive crystals. The dynamic stress–strain curves in compression are shown in Fig. 6b. The high strain rate of $\sim 2.5 \times 10^3\ s^{-1}$ is fairly constant, as demonstrated in Fig. 6c. This was ensured by the use of the pulse shaper. The dynamic yield stresses varied from 350 to 750 MPa and are somewhat higher than the quasi-static values. The compacts with continuous Al phase, W + Al and Ni + Al, have lower dynamic yield stresses, consistent with the quasi-static test results. These quasi-static and dynamic yield stresses are plotted as a function of strain rate in Fig. 7. The nonlinear tendency shown in the dynamic regime (from $10^3$ to $2.5 \times 10^3\ s^{-1}$) for the compacts with Ta, Mo and Nb, showing higher strain rate sensitivities, are a clear consequence of the continuous phase determining the strain rate sensitivity as well as the yield stress. Body-centered cubic (bcc) metals (Mo, Nb, Ta) have a higher strain rate sensitivity at higher strain rates because the flow stress is determined by short-range obstacles (P–N stresses) rather than long range stresses in face-centered cubic (fcc) metals (dislocation forests). The activation volumes for obstacles in bcc crystals are $\sim 1b^3$ ($b$ is the Burgers vector), whereas they are much higher ($10–100b^3$) in fcc crystals. These nonlinear mechanical properties can be quantitatively characterized using the strain rate sensitivity parameter, $m$:

$$m = \frac{\partial \ln \sigma_y}{\partial \ln \dot{\varepsilon}} \tag{2}$$

where $\sigma_y$ is the yield stress, and $\dot{\varepsilon}$ is the strain rate. The strain rate sensitivity of Ta + Al changes from $4.4 \times 10^{-2}$ to $2 \times 10^{-1}$ in the high strain rate regime (about $10^3\ s^{-1}$); however, for the compacts with continuous Al phase there

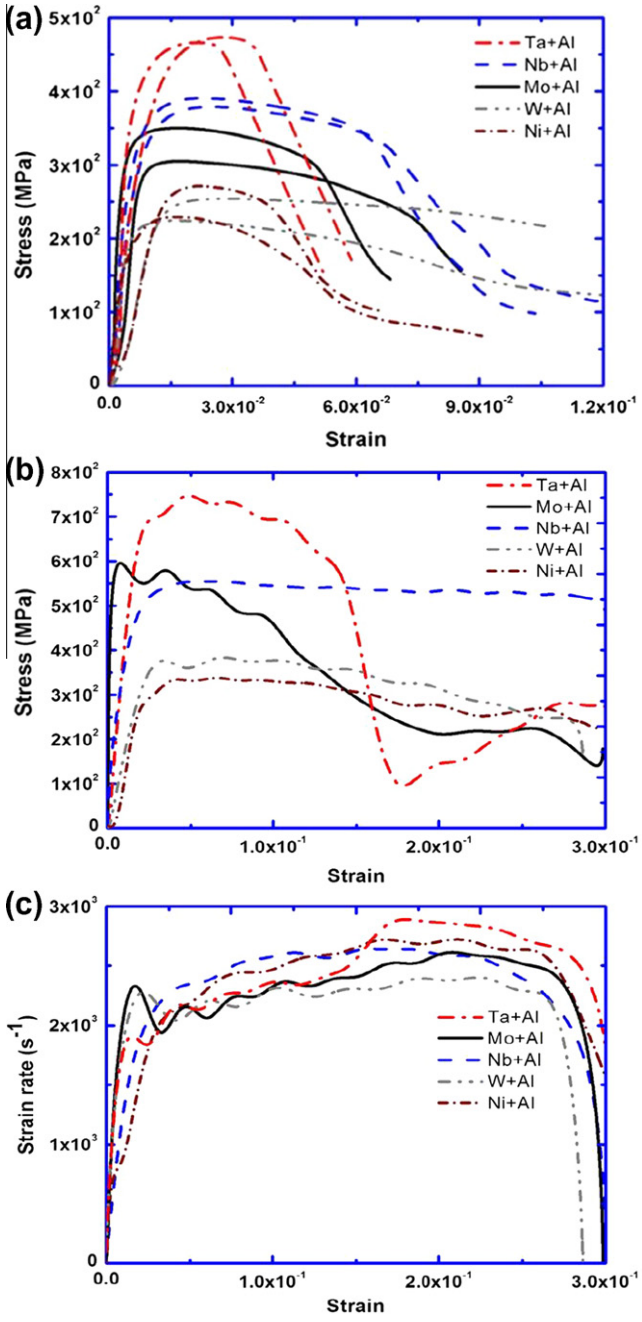


Fig. 6. (a) Quasi-static tests (strain rates $\approx 10^{-3}$ s$^{-1}$); (b) split Hopkinson pressure bar tests (strain rates $\approx 2.5 \times 10^{3}$ s$^{-1}$); and (c) strain rate vs. strain from Hopkinson bar experiments.

is no obvious change of the $m$ value. Hence, the character of the continuous phase is manifested in the mechanical response of the explosively consolidated compacts.

Table 3
Volumetric fractions of micrographs shown in Fig. 4 measured by ImageJ, Hashin–Strikman estimated elastic moduli and estimated yield stress using rule of mixtures of the powder-consolidated compacts.

| Compact | Al phase (vol.%) | Second phase (vol.%) | Hashin–Strikman estimated $E$ (GPa) [25] | Estimated yield stress (MPa) |
|---|---|---|---|---|
| Ni + Al | 51 | 49 | 109.4 | 534.3 |
| W + Al | 61 | 39 | 87.6 | 653.7 |
| Mo + Al | 48 | 52 | 87.5 | 470.6 |
| Nb + Al | 33 | 67 | 72.3 | 712.3 |
| Ta + Al | 40 | 60 | 78.6 | 520.8 |

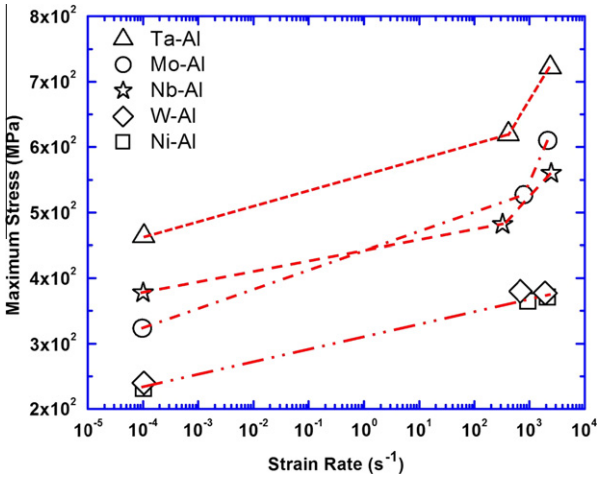


Fig. 7. Maximum stress (flow stress) vs. strain rate of compacts; high strain rate experiments conducted at $\sim 10^{3}$ and $\sim 2.5 \times 10^{3}$ s$^{-1}$.

### 3.3. Characterization of fracture morphology

The sequential images in Fig. 8 show the evolution of damage in the cylindrical specimens subjected to dynamic compression. There are two distinct fracture types: one is the axial splitting fracture parallel to the loading direction on the compacts (Fig. 8a and b); the other is the shear fracture with cracks propagating diagonally at an angle of $\sim 45°$ to the compression direction through the entire sample thickness, as shown in Fig. 8c–e. The axial splitting mode corresponds to the specimens with continuous Al phase: Ni + Al, and W + Al. The shear mode corresponds to the other specimens: Mo + Al, Nb + Al, and Ta + Al, with the continuous bcc metal phase. The cross-sectional SEM images corresponding to the two failures are shown in Fig. 9a–c. The Ni + Al cross-section (Fig. 9a) shows axial splitting failure. However, for the compacts Nb + Al

Table 2
Micro-hardness results for different phases in compacts.

| Compacts | Ni + Al | Ta + Al | W + Al | Mo + Al | Nb + Al |
|---|---|---|---|---|---|
| Hardness (Al) (GPa) | 0.53 ± 0.06 | 0.49 ± 0.04 | 0.55 ± 0.07 | 0.5 ± 0.06 | 0.67 ± 0.16 |
| Element | Ni | Ta | W | Mo | Nb |
| Hardness (Ni, Ta, W, Mo, Nb) (GPa) | 2.7 ± 0.32 | 2.24 ± 0.89 | 4.17 ± 0.24 | 2.21 ± 0.8 | 2.92 ± 0.27 |

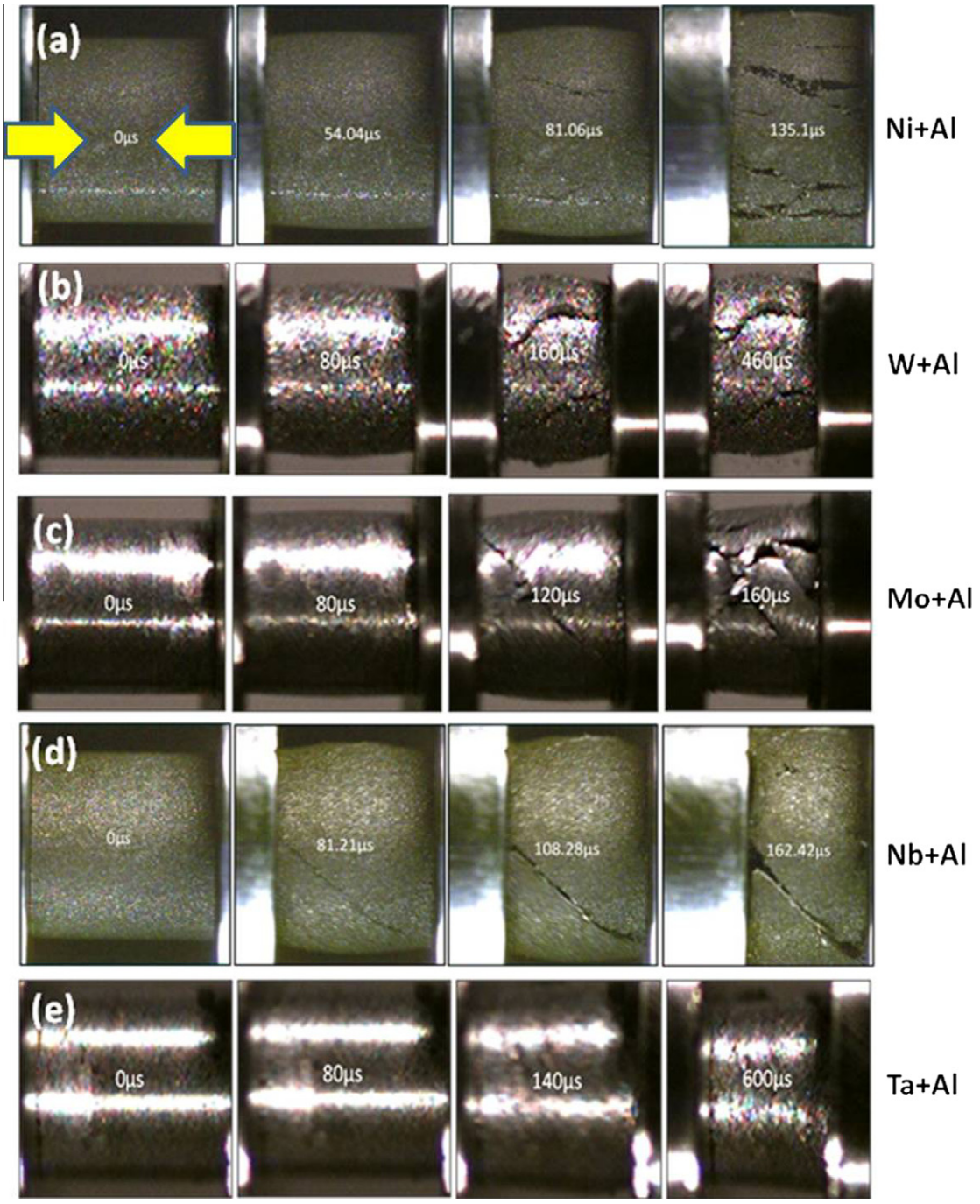


Fig. 8. Snapshots from high-speed cinematography during dynamic compression showing that (a) Ni + Al and (b) W + Al exhibit axial splitting failure, and (c) Mo + Al, (d) Nb + Al and (e) Ta + Al have only shear failure (loading direction horizontal).

and Ta + Al, the propagation direction of the cracks is altered and results in primarily shear failures, as shown in Fig. 9b and c.

The two failure mechanisms and their distinctive microstructures are shown schematically in Fig. 10. Fig. 10a illustrates how the axial splitting failure forms in the compact with the continuous Al phase. The discontinuously distributed second phase particles dispersed in the continuous Al phase can be considered as rigid during plastic deformation in uniaxial compressive loading because their hardness significantly exceeds that of Al. The separation is initiated at the interface between these "rigid" Ni or W particles and the Al matrix. During compression loading, the rigid particles move and cluster in the Al matrix. As the compact continues to be compressed (vertically), these clustered particles are crowded out and move laterally (horizontally), creating gaps. The low bonding strength between particle and matrix enables the creation of cracks with longitudinal axis parallel to the loading direction, as shown in Fig. 10a (right). Eventually, these micro-cracks

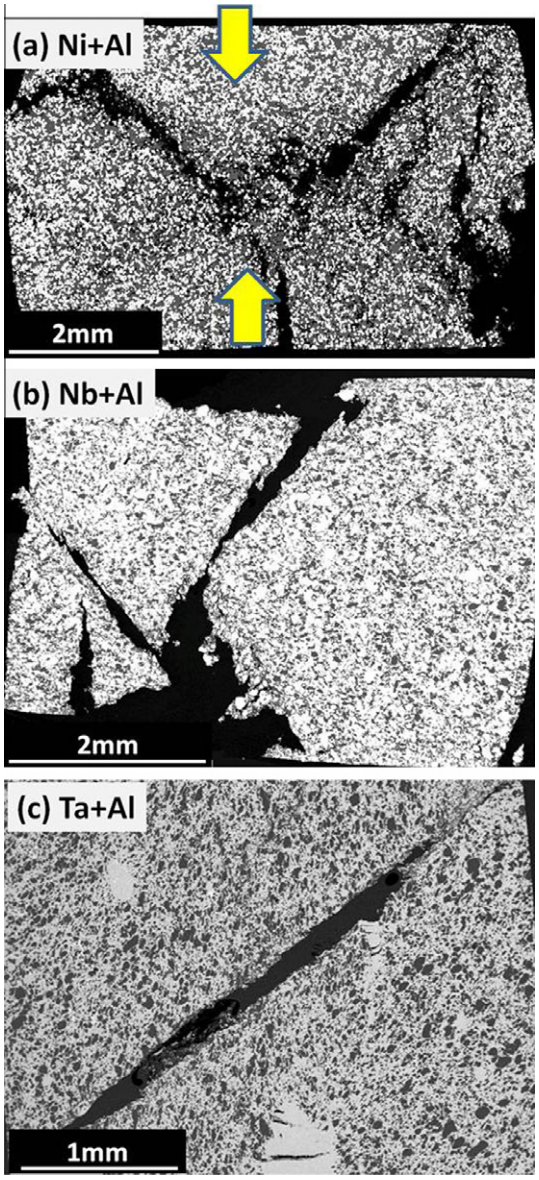


Fig. 9. SEM (BSE) images: (a) Ni + Al, (b) Nb + Al, and (c) Ta + Al samples after dynamic testing corresponding to the different fracture failures, axial splitting (a) and primary shear fracture (b, c), respectively (loading direction vertical).

link and become macro-cracks, propagating through the entire sample as axial splitting. This is shown in the corresponding experimental result of Fig. 10c, for Ni + Al.

Fig. 10b illustrates the shear failure mechanism. In this case, the continuous phase has a higher yield strength than the discontinuous phase (Al). Table 2 shows that the microhardness of Mo, Nb, and Ta is 3–4 times that of aluminum. Thus, as the compact is deformed in compression, the "hard" matrix and the "soft" discontinuous phase combine to enhance shear failure. (Fig. 10b, right inset). The discontinuous phase no longer restricts the shear of the continuous phase, but actually assists it because it has a lower strength. This results in the diagonal shear crack propagation (shown in Fig. 10d) and enhances the mechanical strength of these compacts. Cai et al. [29–31] and Herbold et al. [32–33] found that in the consolidated powder composites, the metallic powder granules with fine particle sizes can tailor the dynamic fracture and enhance the mechanical properties due to the meso-scale force chain formation. This is consistent with our experimental results.

### 3.4. Qualitative analysis

The intermetallic phases are known to be a significant factor for determining the mechanical properties of the composites due to their high strength and low density. In this study, the explosive shock-consolidation process provided low energies, but limited intermetallic formation is a possibility. A qualitative evaluation was conducted using X-ray diffractometry (XRD) and differential thermal analysis (DTA). The XRD analysis (Fig. 11) shows the elements contained in each compact. Except for the Nb + Al compact, these as-produced powder compacts had no intermetallic phases after explosive shock consolidation. The intermetallic phase found in the Nb + Al compact was the $Al_3Nb$, which is the intermetallic that can be formed by SHS from powder mixtures [18]. However, the intermetallic phase in Nb + Al compact did not show any solid evidence of strengthening on the mechanical properties and the XRD peaks showed that this intermetallic phase was in a minor amount.

Differential thermal analysis (DTA) is an important probe for identifying the reaction temperatures in the powder mixtures [16]. Only the Ni + Al and Nb + Al compacts were analyzed because of their low reaction temperatures and stable intermetallic phases, which can be easily detected by DTA analysis [16,35]. Other mixtures were not tested by DTA in this study. DTA was conducted on the original (as-produced), quasi-statically and dynamically compressed samples of the Ni + Al and Nb + Al compacts with a temperature ramping rate 10 °C $min^{-1}$, as shown in Fig. 12. The results for Ni + Al samples show a primary heat exotherm at ~650 °C, representing the formation of the intermetallic $NiAl_3$ according to Ref. [16], which is also commonly seen as the first intermetallic phase formed in Ni/Al self-sustaining reactions [34]. There is a convex region at |~620 °C, prior to the primarily exothermic point, which might indicate that there is an intermixing phase in the as-produced Ni + Al compact. This reactive intermixing phase generates $NiAl_3$ intermetallic before the primary exothermic reaction. After quasi-static and dynamic compression, more defects are produced and the Ni/Al interfaces are drastically decreased, which significantly delays and smoothes the first exothermic peak as shown in Fig. 12a.

The Nb + Al original and recovered samples only show strong endothermic reaction corresponding to Al melting, as shown in Fig. 12b. This means that there is practically no intermixing/reaction produced by the compression tests and the explosive shock consolidation. Indeed, DTA (or differential scanning calorimetry) is used to identify the

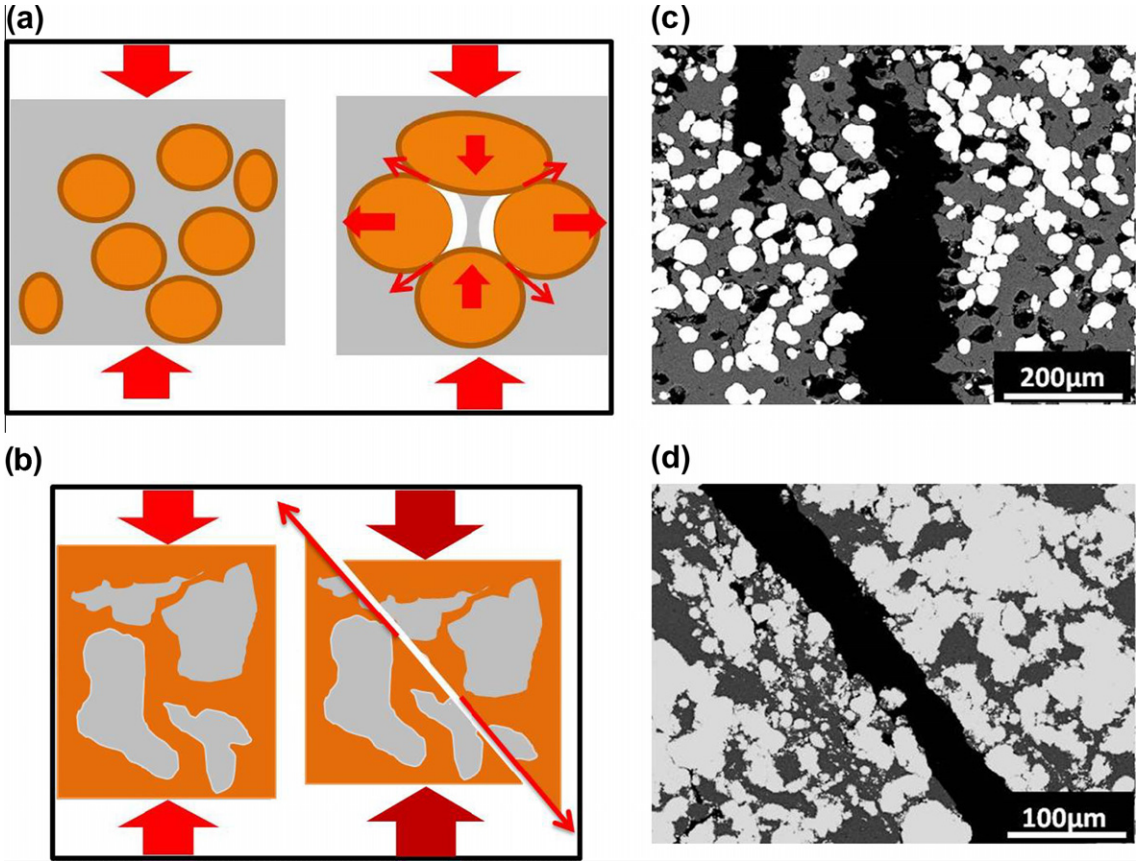


Fig. 10. Schematic of the two failure mechanisms: (a) axial splitting, (b) shear failure, (c) recovered Ni + Al (axial splitting) and (d) Nb + Al (shear failure).

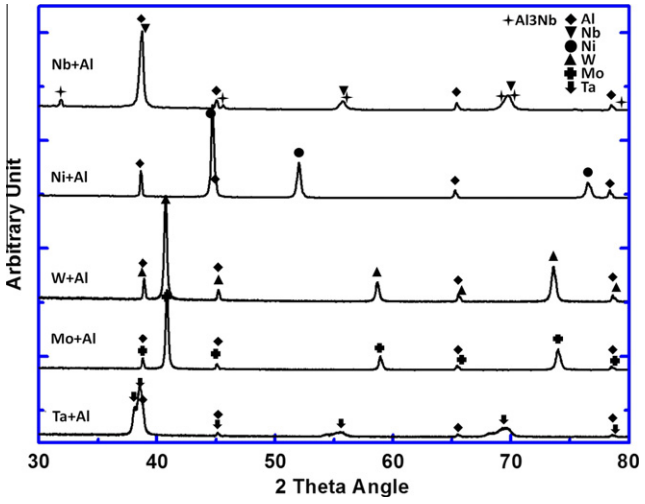


Fig. 11. XRD analysis of as-compacted mixtures.

intermixing layers or pre-existing intermetallics in shock-consolidated or roll-bonded materials [6,35,36].

As the aforementioned qualitative analysis shows, it can be concluded that some intermetallics and intermixing phase pre-existed in the as-produced compacts. However, these heterogeneous phases did not significantly influence the mechanical properties of the explosive shock-consolidated compacts, which was evident in Fig. 6. The mixture without pre-existing intermetallics such as Ta + Al had the highest yield stress, and the one with intermixing phase such as Ni + Al had the lowest yield stress.

### 3.5. Finite element modeling

Finite element (FE) modeling numerical simulations are utilized in order to build a reliable computational model for investigating and predicting the mechanical properties corresponding to failure mechanisms of the explosive consolidated powder mixture compacts. The 2-D simulation code "RAVEN" was used to acquire computational information during dynamic compressing [37]. The yield stress was modeled by using the Johnson–Cook equation:

$$\sigma_y = [A + B(\bar{\varepsilon}^p)^n][1 + C\ln\dot{\varepsilon}^*][1 - T^{*m}] \tag{3}$$

where $A$, $B$, $n$, $C$ and $m$ for nickel, aluminum and tantalum are presented in Table 4 [38–43], and

$$\dot{\varepsilon}^* = \frac{\dot{\varepsilon}}{\dot{\varepsilon}_0} \quad \text{for } \dot{\varepsilon}_0 = 1\ \text{s}^{-1} \quad \text{and } T^* = \frac{\Delta T}{T_{\text{Melt-Room}}} \tag{4}$$

where $\dot{\varepsilon}$ is the strain rate, $\Delta T$ is the temperature change, and $T_{\text{Melt-Room}}$ is the difference between the room temperature and the melting temperature of the materials.

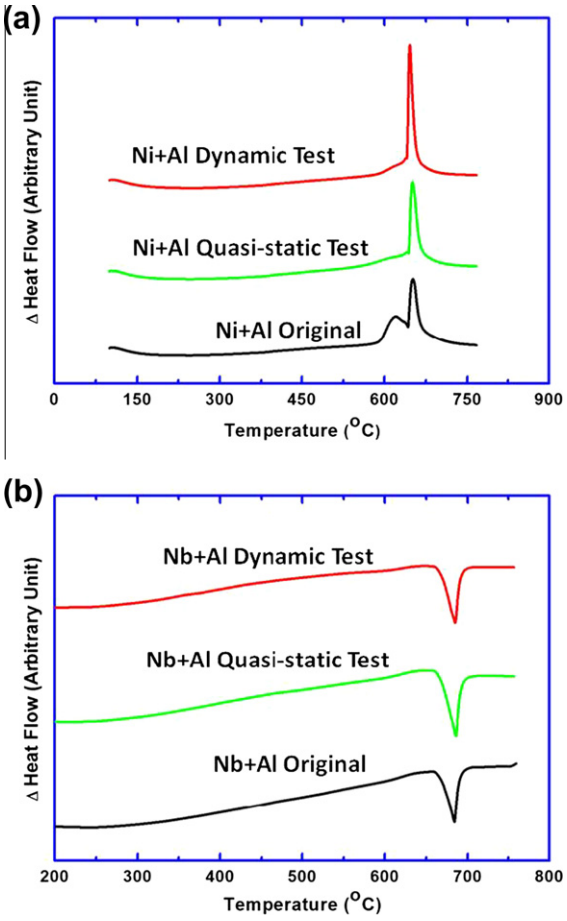


Fig. 12. Differential thermal analysis (DTA) heating curves: (a) original, quasi-statically, and dynamically tested Ni + Al reactive mixtures showing exothermic reaction at ~670 °C; (b) Nb + Al reactive mixtures with the same test conditions as (a). No reaction is observed: endothermic peaks correspond to Al melting.

Table 4
Parameters for Johnson–Cook yield and damage models.

| Parameters | Al | Ni | Ta |
|---|---|---|---|
| $A$ (Mbar) | $1.76 \times 10^{-3}$[a] | $9 \times 10^{-3}$[a] | $7.4 \times 10^{-3}$[a] |
| $B$ (Mbar) | $4.26 \times 10^{-3}$ [42] | $2.4 \times 10^{-3}$[c] | $2.84 \times 10^{-3}$[d] |
| $n$ | 0.1[b] | 0.34[c] | 0.41[d] |
| $C$ | 0.01[b] | 0.006[b] | 0.015[e] |
| $m$ | 1[b] | 1.44[b] | 0.251[e] |
| $T_{melt\text{-}room}$ (K) | 650[b] | 1433[b] | 2957[e] |
| $D_1$ | 0.13[f] | 0[f] | Assuming those are the same as the J–C failure parameters of Ni |
| $D_2$ | 0.13[f] | 4.04[f] | |
| $D_3$ | −1.5[f] | −1.84[f] | |
| $D_4$ | 0.011[f] | 0[f] | |
| $D_5$ | 0[f] | 0[f] | |

[a] Converted from micro-hardness measurements in Table 2.
[b] Obtained from Ref. [37].
[c] Calculated from Ref. [39].
[d] Calculated from Ref. [40].
[e] Obtained from Ref. [38].
[f] Obtained from Ref. [41].

Table 5
Parameters of Grüneisen EOS [42].

| Grüneisen EOS | Al | Ni | Ta |
|---|---|---|---|
| $C_o$ (cm μs$^{-1}$) | 0.5328 | 0.465 | 0.341 |
| $\rho_0$ (g cm$^{-3}$) | 2.768 | 8.902 | 16.65 |
| $S_1$ | 1.338 | 1.445 | 1.2 |
| $S_2$ | 0 | 0 | 0 |
| $S_3$ | 0 | 0 | 0 |
| $\Gamma_0$ | 2 | 1.93 | 1.67 |
| $a_0$ | 0.48 | 0.5 | 0.42 |

The failure strain in Johnson–Cook failure model [43] is specified by the equivalent equation:

$$\varepsilon_f = \lfloor D_1 + D_2 \exp(D_3\sigma^*)\rfloor\lfloor 1 + D_4 \ln \dot{\varepsilon}^*\rfloor\lfloor 1 + D_5 T^*\rfloor \quad (5)$$

where the $D_1$ through $D_5$ are the damage factors which are shown in Table 4, and $\sigma^*$ is the modified stress term defined by the Grüneisen equation of state,

$$P = \frac{\rho_0 C_0^2 \mu[1 + (1 - \frac{\Gamma_0}{2})\mu - \frac{a_0\mu^2}{2}]}{[1 - (S_1 - 1)\mu - \frac{S_2\mu^2}{(\mu+1)} - \frac{S_3\mu^3}{(\mu+1)^2}]^2} + (\Gamma_0 + a_0\mu)E, \text{ for } \mu \geqslant 0 \quad (6)$$

$$P = \rho_0 C_0^2 \mu + (\Gamma_0 + a_0\mu)E, \text{ for } \mu < 0 \quad (7)$$

$$\mu = \frac{\rho}{\rho_0} - 1 \quad (8)$$

where $C_0$, $S_1$, $S_2$, $S_3$, $\Gamma_0$ and $a_0$ are the materials properties of Grüneisen EOS, and $\rho_0$ and $\rho$ are the initial and current density, and $E$ is the energy per reference volume. The parameters of Grueisen EOS and the initial densities are presented in Table 5. The simulation tool used here is employed for investigating its capability to study the mechanical and fracture behaviors of compacts with several different boundary conditions. The parameters for the constitutive equations were obtained from the literature, by converting the microhardness into yield stresses, and taking into consideration the work hardening during the explosive consolidation process. This required the use of work hardening parameters and estimates of the total strain undergone in consolidation. It is important to recognize that the mechanical response of the consolidated components (metal and aluminum) is quite different from the annealed values reported in the literature. They are presented in Tables 4 and 5.

### 3.5.1. Ni + Al simulation

Care was taken to separate all the Ni particles in the computation, even if they touched each other. This procedure effectively assumes that there was no Ni–Ni bonding due to the explosive densification process. In Fig. 13, different Ni particles are represented by different colors, when they touch each other. This initial configuration of the Ni + Al compact was obtained from the SEM observation of the cross-section, shown in Fig. 5a. It contains a volume

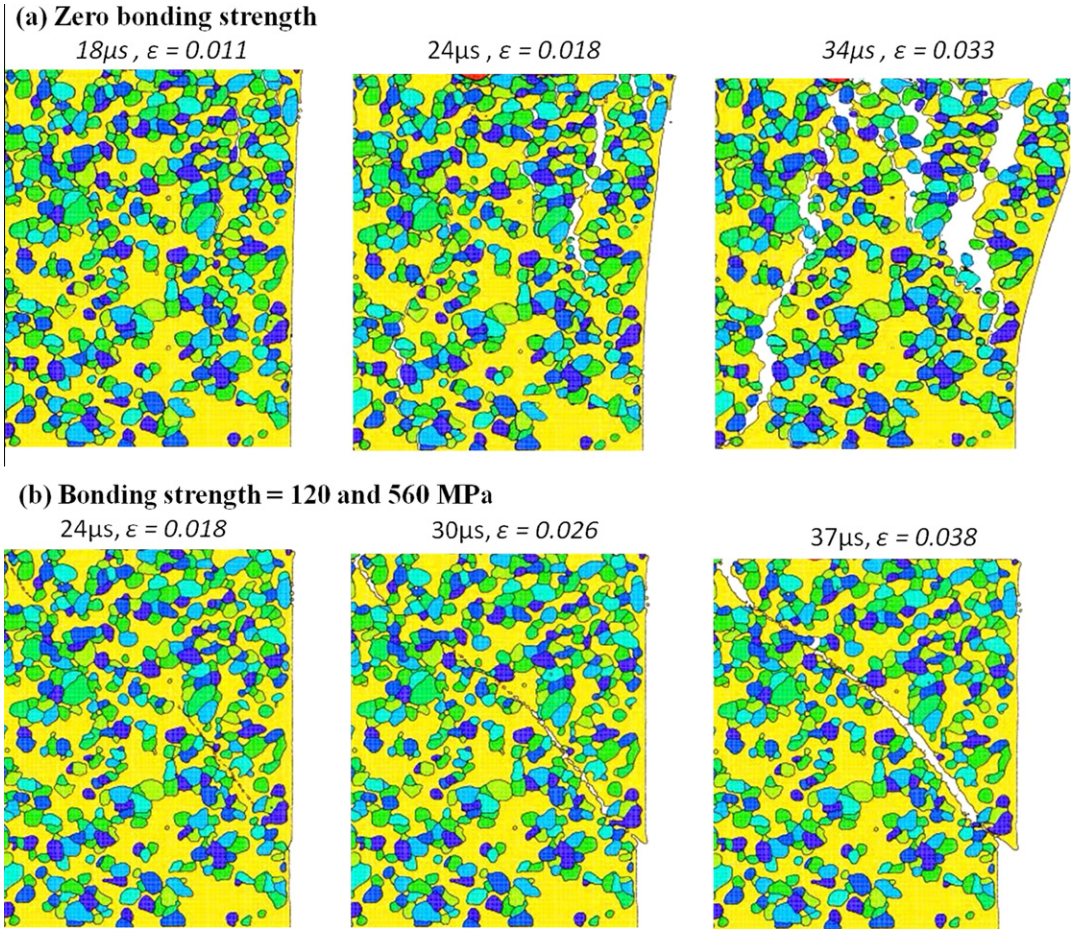


Fig. 13. Compressive deformation of Ni + Al compact: (a) zero bonding strength; (b) 1/2 Al strength (120 MPa) and 560 MPa. $\dot{\varepsilon} \approx 2.5 \times 10^3\ s^{-1}$.

ratio Ni:Al = 56:44, comparable to the meso-scale observation in Table 3. The bonding strength between particles has a definite effect on the evolution of plastic deformation and on the stress–strain response as shown in Fig. 13. Two scenarios are shown: zero bonding strength (Fig. 13a) and bonding strength equal to one half the aluminum yield stress (Fig. 13b). For zero bonding strength, particle separation occurs earlier. It should be noticed that the compressive loading was applied vertically in all simulations.

Fig. 13a shows the simulation results of Ni + Al compact without interfacial bonding strength. The cracks initiated at the interface between Ni particles and Al matrix and are shown as small white areas in Fig. 13a at 18 μs. At a simulation time of 24 μs, these cracks developed and connected to each other, becoming long and narrow cracks aligned parallel to the loading direction. This is the classic process of axial splitting, which is fully developed at 34 μs. On the other hand, if the Ni and Al particles are assumed to be bonded, the mechanism of damage evolution is quite different. Fig. 13b shows the simulation with bonding strengths of 120 and 560 MPa. There is essentially no difference between these two. The process reveals an absence of interface separation at the initial stage as shown in Fig. 13b, at 24 μs. The fracture is initiated in the Al matrix due to the high localized shear strains, Fig. 13b, at 30 μs. At the final stage, Fig. 13b, 37 μs, a shear fracture forms and the compact is completely failed.

The simulation results demonstrate a great consistency in the axial splitting fracture. The interface separation in the simulation result (Fig. 14a) is nearly identical to the experimental observation in Fig. 14b. The stress–strain behavior of the Ni + Al simulations is shown in Fig. 15. Interfacial bonding plays n important role which results in different dynamic yield stresses: ~640 MPa for 120 and 560 MPa bonding strength; ~400 MPa for zero bonding strength. The stress–strain behavior for zero bonding strength Ni + Al compact is consistent with the experimental results in Fig. 6b, which is ~350 MPa. This suggests that the Ni + Al compact was densified by the explosive consolidation without any significant bonding between Ni and Al. On the other hand, the Al-to-Al particles bonded, as demonstrated by the significant compressive strength.

### 3.5.2. Ta+Al simulation

The initial configuration of the Ta + Al compact was imported from the SEM micrograph of the cross-section shown in Fig. 5e. It contains a volume ratio Ta:Al = 70:30, comparable to the meso-scale observation reported in

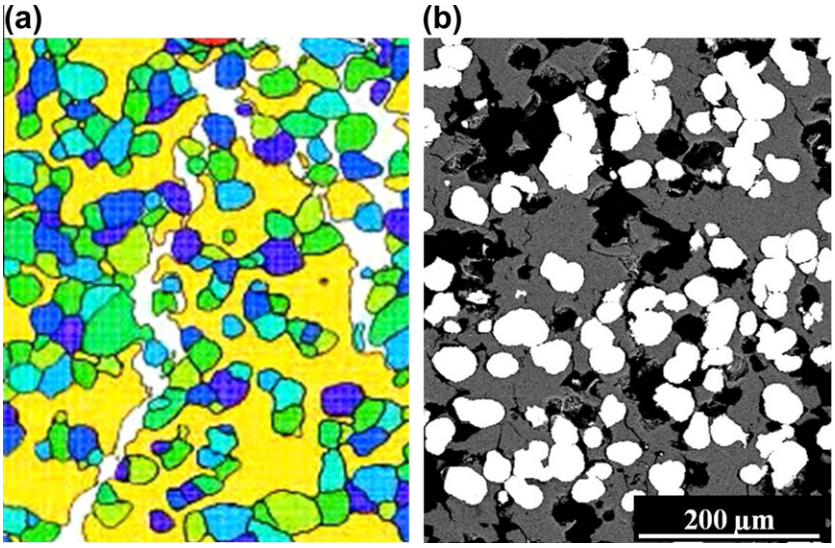


Fig. 14. Compressive deformation of Ni–Al compact. Rigid Ni particles act as barriers to shear and boundary separation leads to microcracks aligned with compression direction: (a) RAVEN simulation; (b) SEM micrograph.

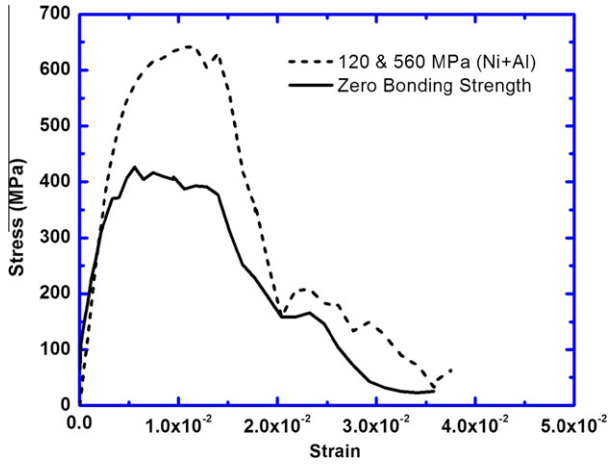


Fig. 15. Simulation results of compressive stress–strain responses for the Ni + Al compact: zero strength, 120 MPa bonding strength (1/2 aluminum strength), and 560 MPa. $\dot{\varepsilon} \approx 2.5 \times 10^3\ s^{-1}$.

Table 3. The situation for the Ta + Al compact is quite different, as shown by the deformation sequences in Fig. 16, which shows Ta + Al compacts with zero, 120 and 560 MPa interfacial bonding strength. Interestingly, the failure mode for different bonding strengths is the same: shear failures are observed for all three different bonding strengths. This implies that in the Ta + Al compacts, the failure evolution is not determined by the interfacial bonding strength. Shear failure initiated from the localized shear deformation of the Al islands surrounded by the Ta matrix, as shown in Fig. 16 at 47 μs simulation time. The localized shear deformation in Al is mainly due to the irregularities of the bulk compressions of the Ta + Al compact, which has the continuous Ta phase with bulk modulus 200 GPa surrounding the Al phase with bulk modulus of 76 GPa. This irregular deformation caused shear fractures that developed into the diagonal shear cracks, as shown in Fig. 16 at 58 μs. Details of the evolution of damage, expressed by the damage parameter (varying from 0 to 1) are shown in Fig. 17.

The stress–strain curves of the three Ta + Al simulations (Fig. 18), confirm that the interfacial bonding strength has no influence on the failure of Ta + Al compacts. Independent of the bonding strength between particles, 0, 120 or 560 MPa, the deformation proceeds by shear localization at ~45° to the compression axis. The process is analogous to the experimentally observed damage evaluations shown in Fig. 8d and e. The Al particles have a much lower strength than Ta (176 vs. 740 MPa). The detail in Fig. 17 shows that this region is quite narrow.

Interestingly, the bonding strength has no effect on the stress–strain response, which shows a flow stress of ~600 MPa comparable with the experimentally observed value at the same strain rate of $2.5 \times 10^3\ s^{-1}$, which is shown in Fig. 6b. It should be pointed out that the compressive strains withstood by the simulations are much lower than the experimental values. The stress drops significantly for $\varepsilon = 0.05$. The experimental maximum strains are on the order of $\sim 10^{-1}$. This difference is, at least partially, due to the size of the specimen, which is about five times larger than the simulation setup. The region modeled by RAVEN has dimensions of $850 \times 600$ μm, whereas the actual specimens have dimensions of $4 \times 3$ mm. Thus, much longer cracks and shear bands can develop prior to failure.

The simulations for Ta + Al are also consistent with the experimental observation. The mechanism of failure is shearing at ~45° to the compressive axis. These shear localization bands eventually cross each other, as seen in Fig. 9b and c. The stress–strain response of the Ta + Al compression simulation is shown in Fig. 18. The stress plateau at 600 MPa is close to the experimental path shown in Fig. 6b.

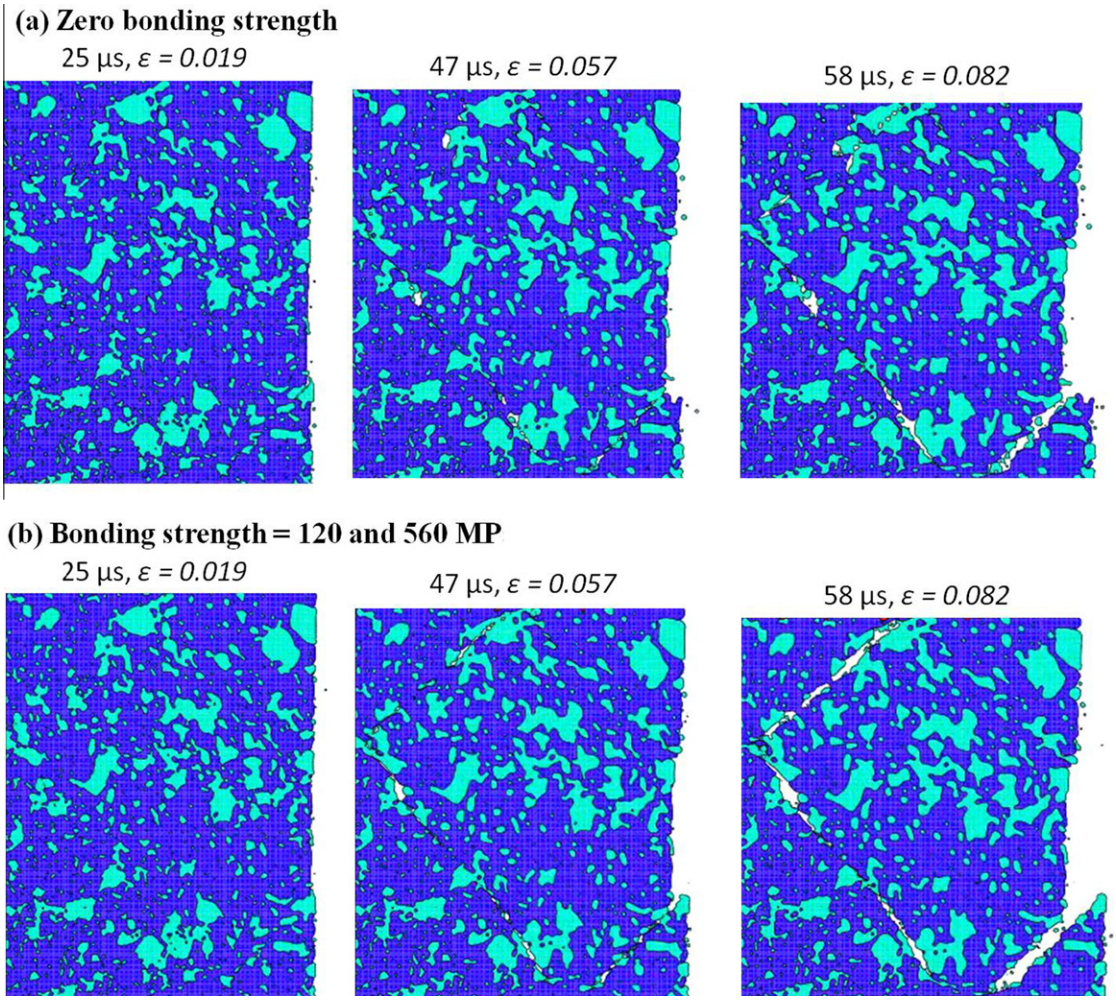


Fig. 16. Compressive deformation of Ta + Al compact: (a) zero bonding strength; (b) 1/2 Al strength (120 MPa) and 560 MPa. $\dot{\varepsilon} \approx 2.5 \times 10^3\ s^{-1}$.

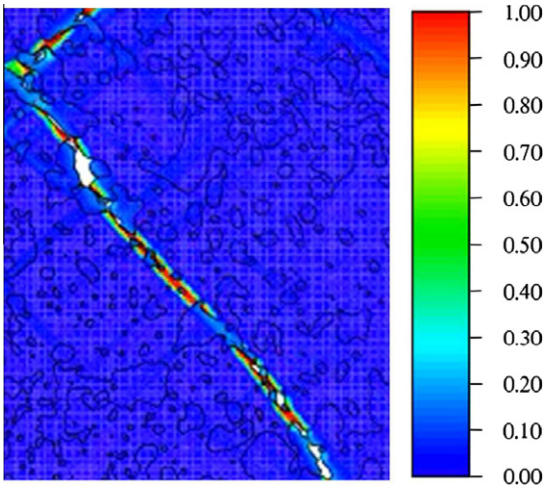


Fig. 17. Damage distribution at 47 μs of TaAl reactive mixture (color bar corresponding to the damage level from zero damage, corresponding to 0, to complete failure corresponding to 1). (For interpretation of the references to color in this figure legend, the reader is referred to the web version of this article.)

The constitutive response of the compressive properties of these composites leaves one unknown that cannot be experimentally determined: the strength at the interface.

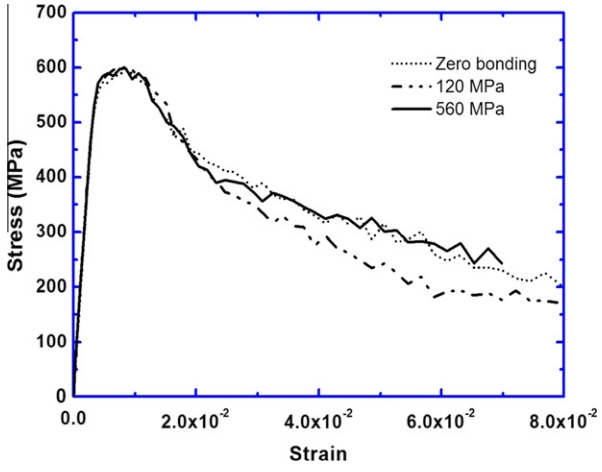


Fig. 18. Simulation results of compressive stress–strain responses for the Ta + Al compact: zero strength, 120 MPa bonding strength (1/2 aluminum strength), and 560 MPa. $\dot{\varepsilon} \approx 2.5 \times 10^3\ s^{-1}$.

Explosive consolidation does not produce perfect bonding between the phases [20]. Indeed, there are regions in which limited melting occurs and thus strengthening the interface bonding. In our experiments, we avoided melting in order to reduce the possibility of shock-assisted reactions as much as possible. Thus the pressure was kept as low as possible to avoid interparticle melting.

## 4. Conclusions

The following are the principal conclusions drawn from the experimental and simulation work performed on explosively consolidated powder mixture compacts:

1. Explosive consolidation in the double-tube cylindrical configuration successfully yielded compacts with varying mechanical strength and a minimum or no reaction between the constituents.
2. The consolidation of Ni and W with Al powder yielded a continuous Al phase in which the other particles were embedded. For Ta, Nb and Mo with Al, the former formed the continuous phase. This is the consequence of the small particle sizes of Ta, Nb and Mo that form agglomerates 50–80 μm in size. These agglomerates can break up and shear during deformation.
3. The mixtures having Al as a continuous phase exhibit a lower strength than the ones with Ta, Mo or Nb as a continuous phase. Hence, the strength is primarily determined by the mechanical properties of the continuous phase.
4. Two mechanisms of failure are identified: shear localization in the continuous phase and tensile separation at the particle–matrix interface. The weak boundary of the interface in the Ni–Al compact leads to axial splitting as a primary failure mode.
5. The Ni + Al and Ta + Al mixtures are modeled by an Eulerian FE modeling code RAVEN and the interfacial strength is shown to have a strong effect on the damage evolution and the strength of the Ni + Al mixture. For the Ta + Al mixture, the mechanical strength and damage evolution are independent of interfacial strength. Failure by both axial splitting and shear localization are predicted by computation, in agreement with experiments.
6. The overall results demonstrate that the strength of the interface between the discontinuous and continuous phases and composition of the continuous phase determine the mechanical properties and failure modes of explosively consolidated compacts of Ni, W, Mo, Nb, and Ta powders with Al.

## Acknowledgements

The authors are thankful to Mr. Daniel Fondse, whose help with preliminary characterization and mechanical testing on the reactive mixtures was essential. They also gratefully acknowledge the assistance from Dr. Eric Herbold with the high-speed camera setup, and Dr. Gustaf Arrhenius with the XRD analysis. This research was supported by the US Navy under the MURI Program (Grant ONR MURI N00014-61007-1-0740).

## References

[1] Sawaoka AB, Akashi T. U S Patent 1987;4:655–830.
[2] Sawaoka AB, editor. Shock compression technology and material science. Tokyo: KTK Scientific Publishers; 1992.
[3] Yu LH, Meyers MA, Thadhani NN. J Mater Res 1990;5:302.
[4] Merzhanov AG. J Mater Process Tech 1996;56:222.
[5] Merzhanov AG, Khaikin BI. Prog Energy Combust Sci 1988;14:1.
[6] Thadhani NN. Prog Mater Sci 1993;37:117.
[7] Taya M. Mater T JIM 1991;32:1.
[8] LaSalvia JC, Kim DK, Meyers MA. Mater Sci Eng 1995;A206:71.
[9] LaSalvia JC, Kim DK, Lipsett RA, Meyers MA. Metall Mater Trans A 1995;26A:3001.
[10] LaSalvia JC, Meyers MA. Matell Mater Trans A 1995;26A:3011.
[11] Vecchio KS, LaSalvia JC, Meyers MA, Gray III GT. Metal Trans A 1992;23A:87.
[12] Hoke DA, Kim DK, La Salvia JC, Meyers MA. J Am Ceram Soc 1996;79:177.
[13] Meyers MA, Wang SL. Acta Metall 1988;36:925.
[14] Du SW, Aydelotte B, Fondse D, Wei CT, Jiang F, Herbold E, et al. Shock compression of condensed matter. AIP Conf Proc 2009;1195:498.
[15] Eakins DE, Thadhani NN. Appl Phys Lett 2008;92:111903.
[16] Dunbar E, Thadhani NN, Graham RA. J Mater Sci 1993;28:2903.
[17] Thiers L, Mukasyan AS, Varma A. Combust Flame 2002;131:198.
[18] Yeh CL, Wang HJ. J Alloy Compd 2009;485:280.
[19] Chen T, Hampikian JM, Thadhani NN. Acta Mater 1999;47:2567.
[20] Meyers MA, Benson DJ, Olevsky. Acta Mat 1999;47:2089–108.
[21] Yang RY, Yu AB, Choi SK, Coates MS, Chan HK. Powder Technol 2008;184:122.
[22] Du SW, Thadhani NN. Shock compression of condensed matter. AIP Conf Proc 2009;1195:470.
[23] Vecchio KS, Jiang F. Metall Mater Trans A 2007;38A:2655.
[24] Budiansky B, O'Connell RJ. Int J Solids Struct 1976;12:81.
[25] Hashin Z. J Appl Mech 1962;29:143.
[26] Arzt E. Acta Mater 1998;46:5611.
[27] Kasiraj P, Vreeland T, Schwarz Jr RB, Ahrens TJ. In: Asay JR, editor. Shock waves in condensed matter, vol. 3; 1984. p.440.
[28] Williamson DM, Siviour CR, Proud WG, Palmer SJP, Govier R, Ellis K, et al. J Phys D Appl Phys 2008;41:085404.
[29] Cai J, Chen Y, Nesterenko VF, Meyers MA. Mater Sci Eng A 2008;485:681.
[30] Cai J, Jiang F, Vecchio KS, Meyers MA, Nesterenko VF. Shock compression of condensed matter. AIP Conf Proc 2007;955:723.
[31] Cai J, Nesterenko VF, Vecchio KS, Jiang F, Herbold EB, Benson DJ, et al. Appl Phys Lett 2008;92:031903.
[32] Herbold EB, Cai J, Benson DJ, Nesterenko VF. Shock compression of condensed matter. AIP Conf Proc 2007;955:785.
[33] Herbold EB, Nesterenko VF, Benson DJ, Cai J, Vecchio KS, Jiang F, et al. J Appl Phys 2008;104:103903.
[34] Qiu X, Graeter J, Kecskes L, Wang J. J Mater Res 2008;23:367.
[35] Ma E, Thompson CV, Clevenger LA. J Appl Phys 1991;69(4):2211.
[36] Coffey CR, Barmak K, Rudman DA, Foner S. J Appl Phys 1992;72(4):1341.
[37] Vitali E, Wei CT, Benson DJ, Meyers MA. Acta Mater 2011;59:5869.
[38] Meyers MA. Dynamic behavior of materials. New York: Wiley; 1994. p. 98–123.
[39] Kim JB, Shin H. Int J Impact Eng 2009;36:746.

[40] Jaramillo VD. A continuous indentation test for metals, M.Sc. thesis, New Mexico Institute of Mining and Technology; 1983.
[41] Chen Y, High strain, high strain-rate deformation of tantalum, Ph.D. thesis, UCSD; 1998.
[42] Johnson GR, Cook WH. Eng Fract Mech 1985;21:31.
[43] Steinberg DJ. Equation of state and strength properties of selected materials. Livermore, CA: Lawrence Livermore National Laboratory; 1996.